Optical and Quantum Electronics (2024) 56:205
https://doi.org/10.1007/s11082-023-05276-9

Modelling and experimental characterization of double layer InP/AlGaInP quantum dot laser

Radwa A. Abbas[1,2] · Yasser M. Sabry[1] · Haitham Omran[2] · Zhihua Huang[3] · Michael Zimmer[3] · Michael Jetter[3] · Peter Michler[3] · Diaa Khalil[1]

Received: 30 January 2023 / Accepted: 5 August 2023 / Published online: 14 December 2023

Abstract
Spectrum of an InP/AlGaInP self- assembled double-layer quantum dot (QD) laser fabricated by metal–organic vapor-phase epitaxy is theoretically and experimentally investigated. A bimodal QD size distribution (small and large QD groups) was detected which is formed during the fabrication. A model is proposed based on rate equations accounting for the superposition of two inhomogeneous QD groups. The total output power and the power spectral density (PSD) of the fabricated QD laser are experimentally characterized at room temperature. The output spectrum is segmented into the sum of two Gaussians curves (super Gaussian) belonging to the small and large QD groups. The peak PSD and the spectral width of each group are extracted and their dependency on the injected current density is analysed. The peak of the large QDs is found to be dominant at small current while the peak of the small QDs dominated at high current alongside a reduction in its spectral width leading to lasing based on them. This behaviour is attributed to the saturation of the large QDs energy levels due to its relatively long radiative lifetime. The experimental analysis is in a good agreement with the theoretical results.

Keywords InP quantum dot laser · Inhomogeneity broadening · Quantum dot rate equation · Super Gaussian

1 Introduction

The evolution of quantum dot (QD) laser in the late'80 s, continues to intrigue the interest of scientists in academia and industry due to its important characteristics of low threshold current, discrete energy states, high-temperature stability and narrow emission line compared to quantum well lasers (Asada et al. 1986; Grundmann and Bimberg 1997; Michler 2017). The importance of QD lasers became more significant following the progress in the self-assembled nanostructure growth (Petroff and DenBaars 1994; Search et al., n.d.; Sugawara et al. 2000). Interestingly the QDs can be operated at different wavelengths by engineering their dot size and composition. For instance, the need for red wavelength laser with the aforementioned characteristics can be met addressing

Extended author information available on the last page of the article

different applications such as visible light communications (Zhang et al. 2019), optical sensing (Gerguis et al. 2019), and quantum technology (Wang et al. 2020).

Red wavelength QD lasers using InP QDs embedded in a GaInP barrier feature a bimodality in QD size (small and large QDs) (Pistol 2004; Porsche et al. 1998, 2000). This effect is related to the substrate miss orientation angle and the different growth conditions such as the surface diffusion, the growth temperature, and the growth rate. In these devices, the expected stable laser threshold with increasing temperature could not be fully observed due to the limited band offsets between the barrier and the QDs. To decrease the probability of the thermal escape of the charge carriers, Al is added into the barrier material and, thus, increasing the charge carrier confinement of the QDs. The amount of Al is tailored as suggested in (Schulz et al. 2009)until reaching the optimum composition of the InP-QD embedded in $(Al_{0.1}\ Ga)_{0.51}$ InP barrier (Huang et al. 2019b) where the difference between the ground and 1st excited state for the small QD group was found to be 13 nm. Nevertheless, the modal gain was limited due to low QD density, weak optical confinement factor, and small modal gain. To overcome these challenges, a solution based on the vertical stacking of QD layer was suggested providing several advantages such as larger gain (Grundmann and Bimberg 1997), possibility of ground-state lasing in small cavities, and larger gain saturation limit (Schmidt et al. 1996). A redshift in the lasing wavelength was observed as the number of the stacked layers increases (Han et al. 2019). Moreover, the stacked layers lead to an increase in the external efficiency (Finke et al. 2021). In (Huang et al. 2019a) two layers of InP QDs in $(Al_{0.1}\ Ga)_{0.51}$InP barriers with a spacer thickness of 6 nm was achieved with a net modal gain of 68.5 cm^{-1} compared to 43.7 cm^{-1} for single layer QD (Huang et al. 2019b), and the peak wavelength shift between two QD groups (small and large) is around 45 nm. Modelling of these important effects, using the rate equations, is crucial for full understanding of the optical properties of the system. The rate equation modelling of the QD laser should account for the discrete energy states and the strong contribution of inhomogeneous behaviour compared to the semiconductor laser (Omran and Khalil 2015). Each QD can be treated as an individual laser system, where the carrier rate equation is written per energy state. For instance, a model for InAs-InP(113)B QD laser emitting at 1.55 μ m was presented in (Grillot et al. 2009) where both the ground-state and the excited state could capture carriers from the wetting layer. This was used to study the effect of different cavity lengths and demonstrate the continuous transition of the lasing wavelength from the ground-state to the excited-state as cavity length decreases. In (Breuer et al. 2011) a QD model was used to describe the two electrically isolated sections of InAs/GaInAs QD laser chip (gain and saturable absorber) and verify the experimental findings of a two-state (ground and excited states) mode-locked emission under reverse biased operation. An InAs/InP QD model was presented (Xiong and Zhang 2019) to study the effect of the spacer thickness and the inhomogeneous broadening on promoting the ground-state lasing.

In this work, a theoretical model and extended experimental investigations are presented for a double-layer $InP/(Al_{0.1}Ga)_{0.51}InP$ QD laser system fabricated by metal–organic vapor-phase epitaxy with a 4 nm spacer thickness (Abbas et al. 2021). A model is proposed based on rate equations accounting for the superposition of two inhomogeneous QD groups (small and large) formed during the fabrication. The output spectrum is segmented into the sum of two Gaussians curves belonging to the small and large QD groups. The peak power spectral density (PSD) and spectral width of each group in the output spectrum are extracted and their dependency on the injected current density is analysed. This model, up to the authors' knowledge, is the first of its kind for the bimodal QD size distribution

reported for InP QD laser systems. The rest of this paper is organized as follows. The multi-mode QD rate equation model is presented in Sect. 2. The detailed structure of the double-layer QD laser along with the fabrication process are described in Sect. 3. The experimental results and parameters extraction are presented in Sect. 4. The theoretical results and comparison to the experiments are discussed in Sect. 5. Finally, the work is concluded in Sect. 6.

2 Multi-mode quantum dot rate equation model

The model is based on accounting for two types of inhomogeneity in the system. The first type is the inhomogeneity between small and large QD groups which was observed in the Atomic Force Microscopic (AFM) images in (Pistol 2004; Porsche et al. 1998; Jörg Porsche et al. 2000; Schulz et al. 2009), while the second type is the inhomogeneity inside each group due to the size variation around the standard QD size. In this model, all QDs are assumed to be spatially isolated and the two QD layers have no interaction between them such that the output of the laser system is the superposition of their individual outputs. Having two layers lead to larger number of QDs and, thus, a larger gain. The QD neutrality is conserved by capturing only e–h pairs with equal lifetimes. The Pauli-exclusion principle and spin degeneracy are respected in the calculations.

The system operation starts by injecting carriers of the pulsed current source into the cladding layer. Then the carriers move towards the active region where they relax from the barrier via the wetting layer. Finally, the carriers are captured by the highest energy level inside each QD, where the carriers can relax to lower levels. The number of energy levels as well as their energetic separation are dependent on the size of the QD. For example, the large QD has multiple energy levels with narrow energetic differences. On the contrary, the small QD size results in fewer number of energy levels with wider separation between them. The presented model assumes that all the carriers injected by the pulsed current source reach the wetting layer, while the lowest energy level (ground states) within each QD is considered. The energy diagram is depicted in Fig. 1 where the wetting layer energy level is (E_2). The ground-state energy levels of the two QD groups are (E_1^S, E_1^L), where $S, L = 1, 2, .., N_{S,L}$ refer to the small and large ones, respectively, and $N_{S,L}$ is total number of QDs. The ground states only are considered inside each QD atom based on the results in (Huang et al. 2019a), where it was quite difficult to identify the excited states. First, the wetting layer collects carriers by an average injected rate (I_{avg}), which resembles the effective current of the input pulsed current source since the model is focused on the steady-state response of the system. For the wetting layer, the charge carriers relax/escape with the time constants τ_{21}^S/τ_{12}^S and τ_{21}^L/τ_{12}^L into/from the QD ground statesE_1^S, E_1^L respectively. This also implies indirect coupling between two QD groups via wetting such that in case a QD re-emits a carrier, the wetting layer may reallocate it to another QD. Once the carrier reaches the ground-state, carrier photon interactions take place either by the stimulated process with gain ($g_{m,1}^S, g_{m,1}^L$); where m is the mode number$= 1,2,3..,N_m$, N_m is the total number of modes, and ($E_{1,ph}^S, E_{1,ph}^L$) are the photon energies; or by the spontaneous emission represented by radiative lifetimes (τ_1^L, τ_1^S). The wetting layer radiative lifetime is(τ_2).

Therefore, the rate equations for the number of carries N and the number of photons S are as follows:

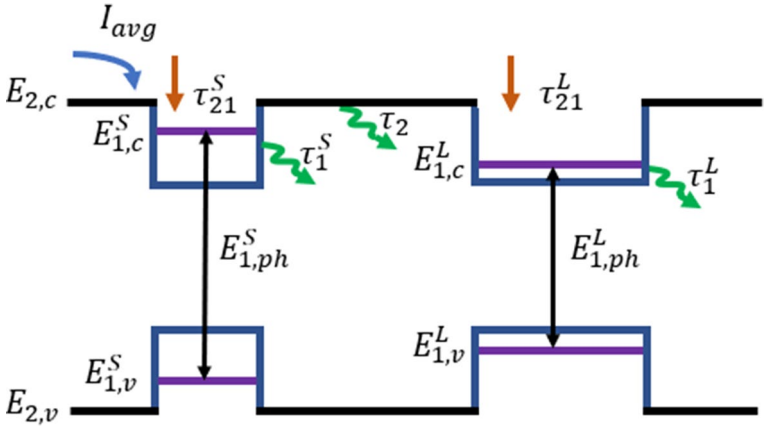

Fig. 1 The energy diagram of a single-layer of the double-layer InP/AlGaInP QD laser showing the different processes starting from the wetting layer energy level

$$\frac{dN_2}{dt} = \frac{I_{avg}}{e} - N_2\sum_L^{N_L}\frac{(1-f_1^L)G^L}{\tau_{21}^L} - N_2\sum_S^{N_S}\frac{(1-f_1^S)G^S}{\tau_{21}^S} - \frac{N_2}{\tau_2} + \sum_L^{N_L}\frac{(1-f_2)N_1^L}{\tau_{12}^L} + \sum_S^{N_S}\frac{(1-f_2)N_1^S}{\tau_{12}^S} \tag{1}$$

$$\frac{dN_1^L}{dt} = \frac{N_2G^L}{\tau_{21}^L}\left(1-f_1^L\right) - \frac{N_1^L}{\tau_1^L} - \frac{(1-f_2)N_1^L}{\tau_{12}^L} - \Gamma_L\sum_m^{N_m} g_{m,1}^L v_g S_m \tag{2}$$

$$\frac{dN_1^S}{dt} = \frac{N_2G^S}{\tau_{21}^S}\left(1-f_1^S\right) - \frac{N_1^S}{\tau_1^S} - \frac{(1-f_2)N_1^S}{\tau_{12}^S} - \Gamma_S\sum_m^{N_m} g_{m,1}^S v_g S_m \tag{3}$$

$$\frac{dS_m}{dt} = \Gamma_L\sum_L^{N_L} g_{m,1}^L v_g S_m + \Gamma_S\sum_S^{N_S} g_{m,1}^S v_g S_m + \beta_L\sum_L^{N_L}\frac{N_1^L}{\tau_1^L} + \beta_S\sum_S^{N_S}\frac{N_1^S}{\tau_1^S} - \frac{S_m}{\tau_{ph}} \tag{4}$$

where N_2 is the wetting layer carriers number, N_1^S and N_1^L are the carriers number for both small and large QDs, S_m is the mode photon number, e is the electron charge, f_2, f_1^S and f_1^L are the occupation probability of the wetting layer and the ground states of the small and large QDs, respectively, G^S and G^L are the inhomogeneous distribution of the small and large QDs, respectively, v_g is the group velocity that is constant for all cavity modes assuming a single transverse mode, Γ_S and Γ_L are the optical confinement factors for the small and large QDs, respectively, and β_S and β_L are spontaneous emission coefficients for the small and large QDs, respectively. The photon lifetime is given by $\tau_{ph} = 1/v_g\left[\alpha_{in} + \frac{1}{2L}\ln\left(\frac{1}{R_1R_2}\right)\right]$, where L is the cavity length, α_{in} are cavity internal losses, and R_1 and R_2 are the laser facets reflectivity.

The gain expression for each QD group is given by:

$$g_{m,1}^j = \frac{2\pi\hbar e^2\langle R_{eh}\rangle^2 N_{QD}^j}{cn_r\epsilon_o m_o^2}G^j\left(E_j - E_j^o\right)B^j\left(E_m - E_j\right)\left(f_{1,c}^j - f_{1,v}^j\right) \tag{5}$$

where j refers to small and large QDs, $\overline{h} = \frac{h}{2\pi}$ where h is Plank's constant, c is the speed of light n_r is the effective refractive index, ϵ_o is free space permittivity, m_o is electron mass, $\langle R_{eh} \rangle^2$ is the optical transition probability,E_m is the mode energy, and $f_{1,c}^j$ and $f_{1,v}^j$ are the occupation probabilities in the conduction and valence bands, respectively. The inhomogeneous broadening is described by a Gaussian distribution:

$$G^j\left(E_j - E_j^o\right) = \frac{1}{\sqrt{2\pi}\xi_j^o} e^{-\frac{\left(E_j - E_j^o\right)^2}{2\xi_j^{o\,2}}} \tag{6}$$

where E_j^o and ξ_j^o are the center of energy and the spectral width, respectively, and the energy level inside each group is calculated by $E_j = E_j^o - (M-i)\frac{ch}{e2n_rL}$, where $i = 0, 1, 2, \ldots, 2M$ represents the index of the QDs inside each group and $2M + 1 = N_S = N_L$ is the total number of the QDs for the small or the large QD group. For the difference in the probability of occupation term$\left(f_{1,c}^j - f_{1,v}^j\right)$, the QD neutrality implies that$f_{1,c}^j = \left(1 - f_{1,v}^j\right)$. Thus $\left(f_{1,c}^j - f_{1,v}^j\right) = \left(2f_{1,c}^j - 1\right)$ where the carrier probability of occupation is assumed to have a non-thermal carrier distribution by $f_1^j = \frac{N_1^j}{2*N_{QD}^j}$ we followed these assumptions as we are concerned with theoretical study for room temperature as supported by (Dogru et al. 2022; Ehlert et al. 2021; Izadyar et al. 2018; Jiang et al. 2019; Quirce and Virte 2022; Xiong and Zhang 2019; Zhou et al. 2020). An interesting method was suggested by (Hutchings et al. 2014) to study whether the carrier distribution is best fitted by non-thermal or thermal distribution based on measurements of the modal gain and spontaneous emission versus temperature. However, the non-thermal carrier distribution assumption is used in this work due its simplicity and focusing the study on the bimodal behaviour at room temperature. As will be shown in the experimental results section, the inhomogeneous broadening is in the range of (40–48 nm) for the large QD envelope and (15–5 nm) for the small QD, while the homogenous broadening is usually much smaller than these values. Therefore, it is assumed that the inhomogeneous broadening is to be the dominating effect in the model, the homogeneous broadening is approximated to be$B^j\left(E_m - E_j\right) = \delta_{mj}$, where δ_{mj} =1 when $m=j$ and zero otherwise.

The QD density in each group is given by:

$$N_{QD}^j = N_{QD} X_j G_n^j \left(E_j - E_j^o\right)\zeta \tag{7}$$

where N_{QD} is the total QD density that is divided between small and large QD groups by a factor X_j, $G_n^j\left(E_j - E_j^o\right)$ is the normalized Gaussian distribution, where $\sum^j G_n^j = 1$, and ζ is the ratio between the covered area of the QDs to the total area of the cavity.

The escape lifetime relation is defined by (Markus et al. 2003):

$$\tau_{12}^j = \tau_{21}^j \frac{2N_{QD}X_j}{D_{WL}} e^{\frac{E_{WL} - E_1^j}{K_B T}} \tag{8}$$

where D_{WL} is the number of carriers in the wetting layer.

Finally, the mode output power observed at the output is expressed by:

$$P_m = \frac{1}{2} E_m S_m \frac{v_g}{2L} \ln\left(\frac{1}{R_1 R_2}\right) \tag{9}$$

3 Fabrication of the QD laser

The detailed fabrication steps and layer stack of the QD laser under study are described in this section. The double-layer structure is grown by metal–organic vapor-phase epitaxy (MOVPE) on an n-doped (100)-GaAs substrate with a misorientation angle of 6° -towards the $[111]_A$ direction. An AIX-200 horizontal reactor is used for the epitaxial growth with standard precursors (trimethylgallium, trimethylindium, trimethylaluminum, arsine, and phosphine), at a temperature of 710 °C and a reactor pressure of 100 mbar. The epitaxial structure shown schematically in Fig. 2 is a separate confinement heterostructure (SCH). The n-side doped with silicon consists of a 350 μ m GaAs substrate, 50 nm GaInP buffer layer and an AlInP cladding layer of 1000 nm. The intrinsic active area contains a layer of 2.1 monolayers (ML) of InP QDs separated by a $(Al_{0.1}Ga)_{0.51}InP$ spacer layer of 4 nm from another 2.1 ML layer of InP QD in order to configure the double-layer active region inside the two 10-nm $(Al_{0.1}Ga)_{0.51}InP$ barrier layers embedded within a 300 nm $(Al_{0.55}Ga)_{0.51}InP$ layer. The p-side consists of a similar layer stack as the n-side but doped with Zn. The structure is completed by a 200 nm GaAs contact layer on which the p-metal contact is formed. In the last step the processed sample is cleaved into cavities with a length of 1.08 mm.

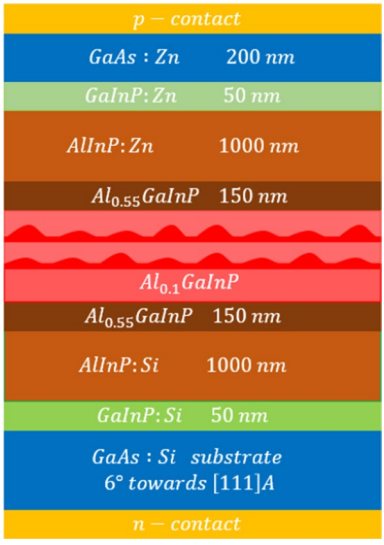

Fig. 2 Schematic drawing of the epitaxial layers (not to scale) for the fabricated double-layer InP/AlGaInP QD laser chip

4 Experimental study

This section presents an experimental study of the double-layer InP/AlGaInP QD laser chip described in Sect. 3 at room temperature. First, the average output power versus the average injected current densities is measured for different duty cycles of the injected pulsed current. Then, for a 0.1% duty cycle the spectral features of the system are investigated, while the average injected current density is increased. The experimental setup is shown in Fig. 3a. The setup consists of a Newport/ILX Lightwave LDP-38408 pulsed current source with two gold-coated tungsten probes. The double-layer InP/AlGaInP QD laser chip is fixed on a bras base thermally connected to a Lightwave LDT-5910C thermos-electric cooler (TEC) operating at room temperature. A cleaved 100-μ m core diameter multimode (MM) fiber is located on a 5-axis positioner and used to couple the output light from the chip to Yokogawa AQ6370 optical spectrum analyser (OSA) or to Newport 1918–D power meter (PM). A microscope camera image is shown in Fig. 3b showing the gold-coated tungsten probe that is used for the electrical connectivity of the pulsed current and the laser chip, the double-layer InP/AlGaInP QD laser chip is fixed on a bras base thermally connected to a TEC, and the cleaved 100 μ m core diameter multimode (MM) fiber.

In Fig. 4 the average output power detected using the PM versus the average injected current density is depicted at three different duty cycles of 0.075%, 0.1%, and 0.15%. The extracted thresholds were found to be 0.47 A/cm^2, 0.63 A/cm^2 and 0.97 A/cm^2, respectively, based on linear extrapolation of the super threshold region. The increase in the average threshold current density and in the average power as the duty cycle increases can be attributed to the thermal escape of the carriers and the excitation of higher energy levels leading to larger overall output power (Hofstetter et al. 2001). The slope efficiency is almost unaffected by the change in duty cycle and has a value of about 0.2 W/A. The average power measured is relatively low for a chip length of 1.08 mm, that can be attributed to the direct coupling loss between the chip and the fiber.

The chip output spectrum is recorded for different excitation average current densities and 0.1% duty cycle as shown in Fig. 5. The spectrum analyser resolution is adjusted at 50 pm in Fig. 5c and at 2 nm for the rest of figures. The operation can be divided into three regimes. As shown in Fig. 5a, the first regime spans average current densities from 0.46 to 0.65 A/cm^2, where the emission from the large QDs dominates the spectrum. The peak is around 710.7 nm at a full width half maximum (FWHM) of 72 nm for 0.46 A/cm^2. The

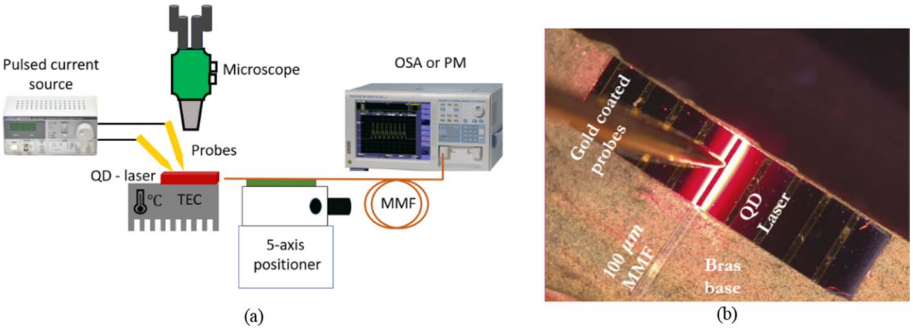

Fig. 3 **a** The experimental setup used to obtain the measurement result. **b** Microscope camera image of the probe, the QD laser chip fixed on a bras base and the cleaved multimode fiber

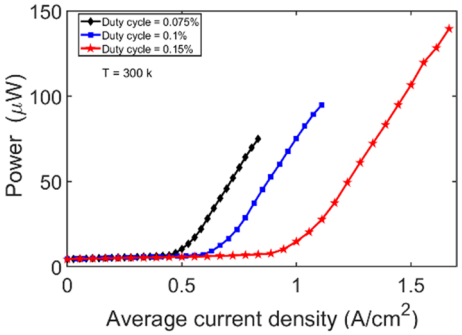

Fig. 4 Average output power of the double-layer InP/AlGaInP QD laser chip versus average injected current densities for 0.075%, 0.1% and 0.15% duty cycle at room temperature

second regime spans average current densities from 0.74 to 0.83 A/cm^2, where the emission intensity from the small and large QD groups is in the same order. The peak of the small QD group is centred on $\lambda = 672$ nm at 0.74 A/cm^2. The third regime is at average current densities larger than 0.83 A/cm^2. As shown in Fig. 5b starting from 0.93 A/cm^2, the contribution of the small QD group dominates and the spectral peak is shifted to about 665.6 nm with a drop in the FWHM to about 7.34 nm which hints to amplified emission. There is a difference in the spectral peak between first and third regions of $\Delta\lambda$peak = 45.1

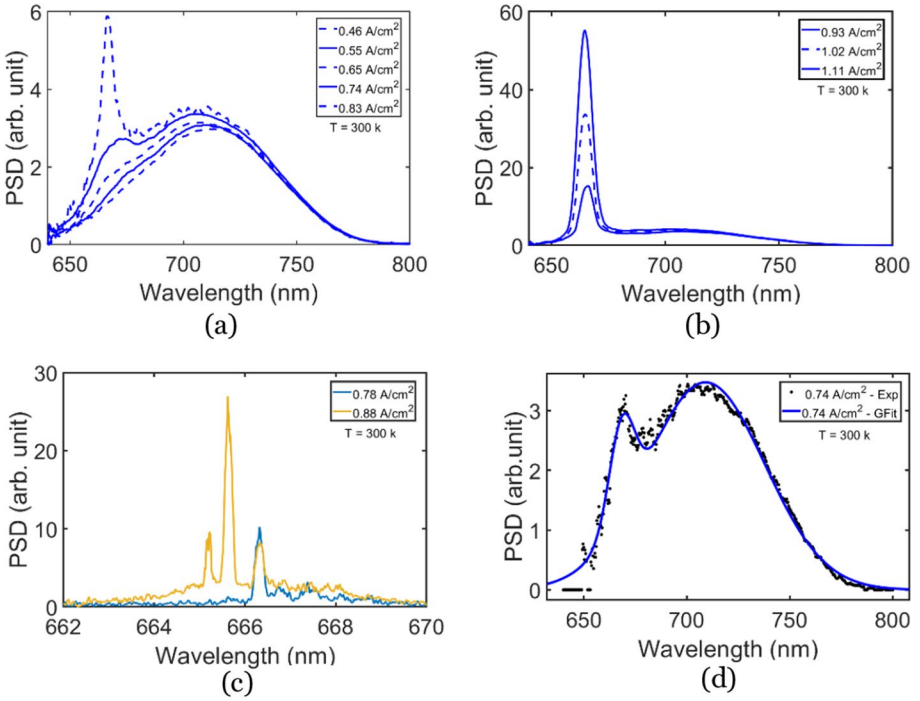

Fig. 5 PSD versus wavelength for different current densities for 0.1% duty cycle at room temperature. **a** Average current densities from 0.46 to 0.83 A/cm^2 **b** Average current densities 0.93 A/cm^2 and above. **c** A closer look at the spectrum for current densities of 0.78 A/cm^2 and 0.88 A/cm^2. **d** The PSD versus wavelength at 0.74 A/cm^2 current density showing the measured and the Gaussian fitting data (GFit)

nm or ΔEpeak = 118.3 meV that is consistent with the results in (Huang et al. 2019a). Fig. 5c shows a closer look of the spectrum around the small QD peak wavelength for two different current densities above the threshold. The linewidth of the central line is about 0.17 nm at 0.88 A/cm^2 average current density.

Fitting of the spectra with two Gaussian curves is used for the extraction of the peak PSD and the spectral width of each QD group as shown in Fig. 5d. The following fitting relation is used:

$$PSD = a_S e^{-\left(\frac{\lambda - b_S}{c_S}\right)^2} + a_L e^{-\left(\frac{\lambda - b_L}{c_L}\right)^2} \tag{9}$$

where $a_{S,L}$ is peak PSD amplitude, $b_{S,L}$ is the centre wavelength and $c_{S,L}$ is the spectral width. The subscripts S and L refers to the small and large QDs, respectively. In Fig. 6a and b, the extracted $a_{S,L}$ and $c_{S,L}$ are plotted, respectively, versus the injected average current density. The small QD group peak PSD increases, and the spectral width decreases as the injected current density increases following the lasing behaviour. On the other hand, the large QD group peak PSD barely increases, and the spectral width increases with the applied injected current density emphasizing the saturation behaviour. This analysis indicates that the lasing occurs via the small QD group only.

These observations could be explained as follows. In the first regime, where the large QDs dominate the spectrum, the small energy separation of the excited states for the large QD group facilitates the transfer of the carriers from the wetting layer to the ground-state in shorter time compared to the small QDs (Grosse et al. 1997; Roßbach et al. 2008). However, in the second and third regimes, the small QDs start lasing, while the large QDs saturate as shown in Fig. 5a. This is because of the higher modal gain of the small QDs compared to the larger ones (Huang et al. 2019a). Even at low injected average current density the luminescence of the large QDs saturate and the ensemble spectra start to shift to shorter wavelength (Fig. 5a). This state filling behaviour is a consequence of a weak wave function overlap between electrons and holes, resulting in a long charge carrier lifetime (Laheld et al. 1995). The charge carrier in the small QDs exhibit a stronger wavefunctions overlap and thus recombine much faster which lead to a higher emission intensity in the higher energy spectral range.

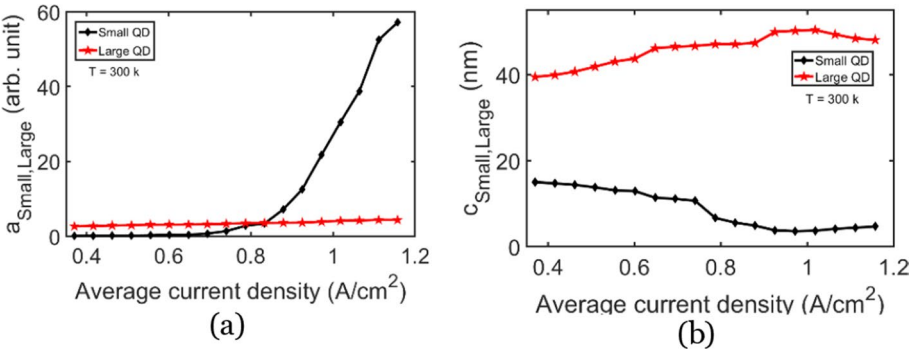

Fig. 6 Extracted information for the small and large QD groups from the Gaussian fitting versus average current densities. **a** The peak PSD amplitude of the Gaussian fit. **b** The spectral width of the Gaussian fit

5 Model results and discussion

The model equations presented in Sect. 2 are solved numerically using Runge–Kutta method for solving the nonlinear differential equations with a simulation time duration of 10 ns. The values of the different parameters are listed in Table 1. The effect of the two uncorrelated QD layers is reflected in the increase of the QD density compared to the single layer (Huang et al. 2019b), and is set to be $N_{QD} = 1.6\text{x}10^{10}\text{cm}^{-2}$ which results in the expected increase of the gain, while ζ, which is the ratio between coverage area of the QDs to the total area of the cavity is set to be 1/5. Although, the QD structure is best described to be a truncated pyramid, the solution of such a system is complicated and no analytical formula was found to describe it. Early (Califano and Harrison 2000) and more recent (Nenashev and Dvurechenskii 2020) research papers studies numerical methods to solve such a complex system. The QD structure in this work is approximated to be a cylindrical QD with an infinite potential barrier and the dimensions of the small and large QDs are extracted from the corresponding peak energies. This is to acquire an approximate value of the ratio between the dimensions that the rate equation model parameters depend on such as the optical confinement factor and the spontaneous emission factor. The relation used for the energy levels in a cylindrical QD assuming an infinite barrier height is $E = E_g + \frac{\hbar^2}{2m^*}(\frac{k_0^2}{R^2} + \frac{\pi^2}{H^2})$ (Liu and Xu 2008), where R is the radius, H is the height, m^* is the effective mass and k_0 is the first zero of the zero order Bessel function of the first kind. Given that the emission wavelengths of the small and large QDs are 672 nm and 710.7 nm, respectively, the corresponding energies are about 1.85 eV and 1.75 eV, respectively. Geometrically, the aspect ratios of the small and large QD cylinders are expected to be the same value of about ~ 10 owing to the fabrication process. Thus, radii and heights of the QDs are calculated and found to be $R^S_{QD} = 16.3\,\text{nm}$ and $H^S_{QD} = 3.3\,\text{nm}$ for the small QD and $R^L_{QD} = 18.3\,\text{nm}$ and $H^L_{QD} = 3.7\,\text{nm}$ for the large QD. Since the optical confinement factor is the mode volume enclosed by the QD relative to the mode volume enclosed by the cavity, hence the ratio between small and large QDs can be approximated to be the ratio between the volume of the two cylinders given by $\Gamma_L = 1.5\Gamma_S$. The spontaneous emission factor is proportional to the optical confinement factor as stated in (Petermann 1979), therefore the spontaneous coefficient factor is set to be $\beta_S = 2.33 \times 10^{-3}$ for the small QDs and $\beta_L = 3.5 \times 10^{-3}$ for the large QDs. The capture time τ_{21} is the model parameter associated with the relaxation of the charge carriers from the wetting layer into the QD ground states. Hence, it is dependent on the energy level spacing of the individual QD and their coupling to the wetting layer. For the smaller sized QDs it was found that they only exhibit one confined electron level, while the larger QDs have at least two (Beirne et al. 2005). This results in a faster capture time for the larger QDs with a pronounced state filling. As already mentioned above, the recombination in the smaller QDs occurs with a higher rate due to the stronger wavefunction overlap, thus the radiative lifetimes for the small QDs are set to smaller values compares to the larger ones. Capture lifetimes for the small and large QDs of $\tau^S_{21} = 12ps$ and $\tau^L_{21} = 2ps$, respectively, and radiative lifetimes for the small and large QDs of $\tau^S_1 = 0.4ns$ and $\tau^L_1 = 2ns$, respectively, give a good match between the experimental results and the model. The radiative lifetime for the wetting later is estimated to $\tau_2 = 2ns$. The extracted spectral width and central wavelength values from (6) are used. Fig. 7a–c show the PSD versus the wavelength obtained from the model simulation and the

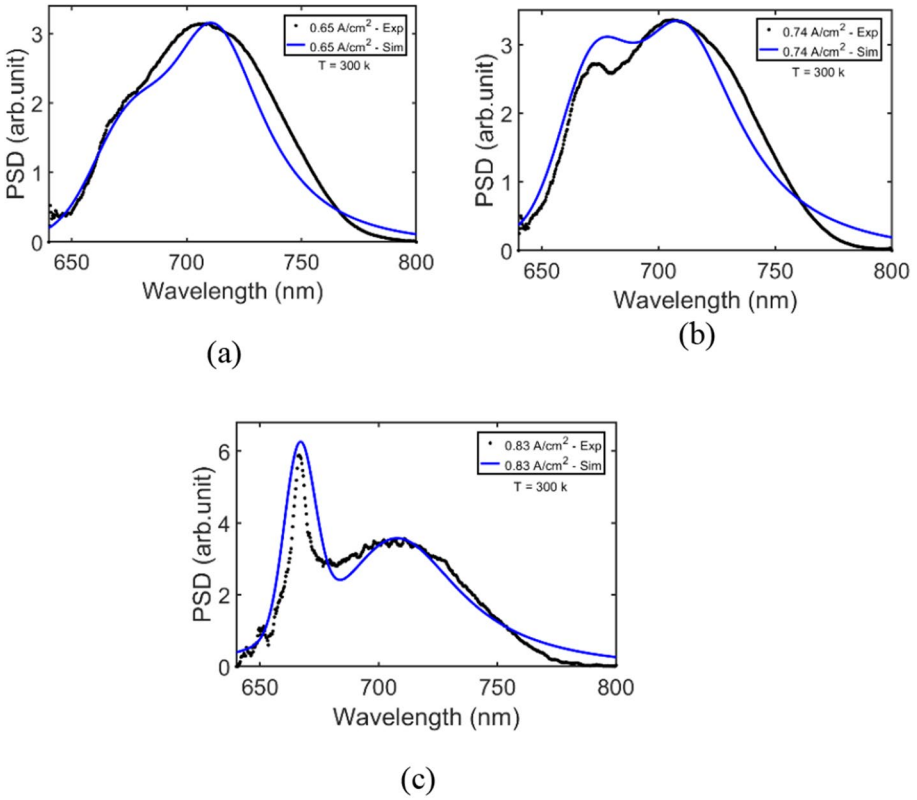

Fig. 7 PSD versus wavelength for the experimental data (dotted black) and simulation results (solid blue) at three different average current densities using 0.1% duty cycle at room temperature. **a** at 0.65 A/cm^2 **b** at 0.74 A/cm^2 **c** at a 0.83 A/cm^2

experimental data for three different injected average current densities resembling the transition between the three regimes discussed earlier in Sect. 4. Fig. 7a shows the spectrum at a 0.65 A/cm^2 average current density, where the large QD group dominates the spectrum. The two Gaussian peaks fitting model is applied to the experimental and simulation data and their results are compared. The percentage error in the amplitude of the small and large QDs is about 1.58 % and 1.8 %, respectively, while the percentage error in the spectral width is about of 5 %, and − 3.2 %, respectively. Fig. 7b shows the spectrum at an average current density of 0.74 A/cm^2. The percentage error in the amplitude of the small and large QDs is 7.4 % and 0.44%, respectively, while the spectral width error is 10 % and − 4.6%, respectively. Finally, Fig. 7c shows the spectrum at an average current density of 0.83 A/cm^2, where the small QD group dominates the spectrum. The calculated percentage error in the amplitude and spectral width is about 9.8 % and 5.8 %, respectively, for the small QD; and − 4.9 % and − 2.3 % for the large QD. Therefore, an overall good match between the theoretical and the experimental results is obtained for the different average current densities.

Table 1 model parameter

Parameter's name	Symbol	Quantity (unit)	Parameter's name	Symbol	Quantity (unit)
Temperature	T	300 (K)	Small QD height	H_{QD}^{S}	3.3(nm)
Chip length	L	1080(μm) Huang et al. (2019b)	Small QD optical confinement factor	Γ_S	3.33%
Cross sectional area	A	$1.08 \times 10^{-3}\left(\mathrm{cm}^2\right)$ Huang et al. (2019b)	Small spontaneous emission coupling factor	β_S	2.33×10^{-3}
Coverage area ratio	ζ	*1/5*	Small QD capture time	τ_{21}^{S}	12(ps)
Modes number	N_m	2177	Small QD radiative lifetime	τ_1^S	0.4(ns)
Total QD number	$2M+1$	2177	Large QD centre energy	$E_1^{L,0}$	1.75(ev)
Total QD density	N_{QD}	$1.6 \times 10^{10}(\mathrm{cm}^{-2})$	Large QD contribution	X_L	75%
Internal cavity losses	α_{int}	$4(\mathrm{cm}^{-1})$	Large spontaneous emission coupling factor	β_L	3.5×10^{-3}
Effective refractive index	n_r	3.218 Huang et al. (2019b)	Large QD height	H_{QD}^{L}	3.7(nm)
Facet reflectivity	R_1, R_2	0.276 Huang et al. (2019b)	Large QD radius	R_{QD}^{L}	18.3(nm)
Energy gap	E_g	1.344(eV) Levinshtein et al. (2000)	Large QD optical confinement factor	Γ_L	5%
Electron effective mass	m_e^*	$0.08m_o$ Levinshtein et al. (2000)	Large QD capture time	τ_{21}^{L}	2(ps)
Small QD centre energy	$E_1^{S,0}$	1.85(ev)	Large QD radiative lifetime	τ_1^L	2(ns)
Small QD contribution	X_S	25%	Wetting layer energy	E_2	1.91(ev)
Small QD radius	R_{QD}^{S}	16.3(nm)	Wetting layer Density	D_{WL}/A_{QD}	$1.68 * 10^9(\mathrm{cm}^{-2})$
Electron effective mass	m_e^*	$0.08m_o$ Levinshtein et al. (2000)	Wetting layer radiative lifetime	τ_2	2(ns)

6 Conclusion

The experimental examination of a double-layer $InP/(Al_{0.1}Ga)_{0.51}InP$ QD laser system was presented showing the co-existence of small and large QDs, while the lasing occurred via the small QD only. For the first time in literature, up to the authors' knowledge, a model for the InP QD laser was presented that also accounted for the bimodal QD size distribution. Two peaks Gaussian fitting model was applied to data extracting the central wavelengths of the emission and the percentage contribution of the small and large QDs in the emission. The size of the QDs was estimated from emission peak wavelengths together with the eigenvalue's solution of cylindrical shape QDs with an infinite barrier height. The theoretical model described the phenomena as the superposition of two inhomogeneous QD groups. The simulation results were compared to the experimental data and percentage errors in the range of 1.5% up to 10% were achieved showing a good agreement.

Authors' contributions RAA performed all the experimental and simulation work and contributed to the writing of the manuscript. YMS contributed to writing the manuscript and supervised the overall work. HO supervised the experimental results. ZH, MZ, MJ, and PM fabricated the laser chip under study, contributed to the analysis of the results, and contributed to the theoretical model. DK supervised the overall work. All authors reviewed the manuscript.

Funding Open access funding provided by The Science, Technology & Innovation Funding Authority (STDF) in cooperation with The Egyptian Knowledge Bank (EKB). The corresponding author is affiliated with an Egyptian institution "Ain Shams University", and "German University in Cairo" where each of them is a participating Egyptian institution as defined by the open access agreement.

Data Availability There were no public data used in this work.

Declarations

Conflict of interest There are no conflict of interest in this submission.

Ethical approval This restructuration is not applicable to this submission as there were no experiments preformed on any humans or animals.

References

Abbas, R.A., Omran, H., Sabry, Y.M., Huang, Z., Zimmer, M., Jetter, M., Michler, P., Khalil, D.: Subthreshold spectral Bi-modality of double layer InP/AlGaInP quantum dot laser. Conf. Digest. IEEE Int. Semicond. Laser Conf. **2**(2), 2–3 (2021). https://doi.org/10.1109/ISLC51662.2021.9615880

Asada, M., Miyamoto, Y., Suematsu, Y.: Gain and the threshold of three-dimensional quantum-box lasers. IEEE J. Quantum Electron. **22**(9), 1915–1921 (1986). https://doi.org/10.1109/JQE.1986.1073149

Beirne, G.J., Michler, P., Jetter, M., Schweizer, H.: Single-photon emission from a type-B InP/GaInP quantum dot. J. Appl. Phys. (2005). https://doi.org/10.1063/1.2130887

Breuer, S., Rossetti, M., Drzewietzki, L., Bardella, P., Montrosset, I., Elsaser, W.: Joint experimental and theoretical investigations of two-state mode locking in a strongly chirped reverse-biased monolithic

quantum dot laser. IEEE J. Quantum Electron. **47**(10), 1320–1329 (2011). https://doi.org/10.1109/JQE.2011.2165834
Califano, M., Harrison, P.: Presentation and experimental validation of a single-band, constant-potential model for self-assembled InAs/GaAs quantum dots. Phys. Rev. B Condens. Matter Mater. Phys. **61**(16), 10959–10965 (2000). https://doi.org/10.1103/PhysRevB.61.10959
Dogru, N., Tunc, H.S.D., et al.: Gain-switched short pulse generation from InAs-InP (1 1 3)B quantum dot laser excited state. Optics Laser Technol. **148**, 107709 (2022). https://doi.org/10.1016/j.optlastec.2021.107709
Ehlert, J.F., Mugnier, A., He, G., Grillot, F.: Modeling of a quantum dot gain chip in an external cavity laser configuration. Laser Phys. **31**(8), 1–9 (2021). https://doi.org/10.1088/1555-6611/ac1073
Finke, T., Sichkovskyi, V., Reithmaier, J.P.: Quantum-dot based vertical external-cavity surface-emitting lasers with high efficiency. IEEE Photon. Technol. Lett. **33**(14), 719–722 (2021). https://doi.org/10.1109/LPT.2021.3089331
Gerguis, J.O., Sabry, Y.M., Omran, H., Khalil, D.: Spectroscopic gas sensing based on a MEMS-SOA swept fiber laser source. J. Lightwave Technol. **37**(20), 5354–5360 (2019). https://doi.org/10.1109/JLT.2019.2932688
Grillot, F., Veselinov, K., Gioannini, M., Montrosset, I., Even, J., Piron, R., Homeyer, E., Loualiche, S.: Spectral analysis of 1 55-m InAs–InP (113) B quantum-dot lasers based on a multipopulation. Quantum **45**(7), 872–878 (2009)
Grosse, S., Sandmann, J., von Plessen, G., Feldmann, J., Lipsanen, H., Sopanen, M., Tulkki, J.: Carrier relaxation dynamics in quantum dots: scattering mechanisms and state-filling effects. Phys. Rev. B Condens. Matter Mater. Phys. **55**(7), 4473–4476 (1997). https://doi.org/10.1103/PhysRevB.55.4473
Grundmann, M.G.M., Bimberg, D.B.D.: Gain and threshold of quantum dot lasers: theory and comparison to experiments. Jpn. J. Appl. Phys. **36**(6S), 4181 (1997)
Han, I.S., Kim, J.S., Shin, J.C., Kim, J.O., Noh, S.K., Lee, S.J., Krishna, S.: Photoluminescence study of InAs/InGaAs sub-monolayer quantum dot infrared photodetectors with various numbers of multiple stack layers. J. Lumin. **207**, 512–519 (2019). https://doi.org/10.1016/j.jlumin.2018.11.052
Hofstetter, D., Beck, M., Aellen, T., Faist, J., Oesterle, U., Ilegems, M., Gini, E., Melchior, H.: Continuous wave operation of a 9.3 µm quantum cascade laser on a Peltier cooler. Appl. Phys. Lett. **78**(14), 1964–1966 (2001). https://doi.org/10.1063/1.1360225
Huang, Z., Hepp, S., Sittig, R., Jetter, M., Michler, P.: Influence of spacer thickness on the optical properties of vertically stacked InP/AlGaInP quantum dot lasers at the short wavelength. Optics InfoBase Conf. Pap. **140**(2009), 385338 (2019a)
Huang, Z., Zimmer, M., Hepp, S., Jetter, M., Michler, P.: Optical gain and lasing properties of InP/AlGaInP quantum-dot laser diode emitting at 660 nm. IEEE J. Quantum Electron. **55**(2), 1–7 (2019b). https://doi.org/10.1109/JQE.2019.2896643
Hutchings, M., O'Driscoll, I., Smowton, P.M., Blood, P.: Fermi-dirac and random carrier distributions in quantum dot lasers. Appl. Phys. Lett. **104**(3), 10–14 (2014). https://doi.org/10.1063/1.4862813
Izadyar, S.M., Razaghi, M., Hassanzadeh, A.: Quantum dot semiconductor optical amplifier: investigation of amplified spontaneous emission and noise figure in the presence of second excited state. Opt. Quant. Electron. **50**(1), 1–13 (2018). https://doi.org/10.1007/s11082-017-1265-3
Jiang, Z.F., Wu, Z.M., Jayaprasath, E., Yang, W.Y., Hu, C.X., Xia, G.Q.: Nonlinear dynamics of exclusive excited-state emission quantum dot lasers under optical injection. Photonics (2019). https://doi.org/10.3390/photonics6020058
Laheld, U.E.H., Pedersen, F.B., Hemmer, P.C.: Excitons in type-II quantum dots: finite offsets. Phys. Rev. B **52**(4), 2697–2703 (1995). https://doi.org/10.1103/PhysRevB.52.2697
Levinshtein M., Rumyantsev S., Shur M. (2000). Levinshtein M. Rumyantsev S. Shur M. - Handbook series on semiconductor parameters. Volume 1.
Liu, C.H., Xu, B.R.: Theoretical study of the optical absorption and refraction index change in a cylindrical quantum dot. Phys. Lett. Sect. A Gener. Atom. Solid State Phys. **372**(6), 888–892 (2008). https://doi.org/10.1016/j.physleta.2007.08.046
Markus, A., Chen, J.X., Gauthier-Lafaye, O., Provost, J.G., Paranthoën, C., Fiore, A.: Impact of intraband relaxation on the performance of a quantum-dot laser. IEEE J. Select. Topics Quantum Electron. **9**(5), 1308–1314 (2003). https://doi.org/10.1109/JSTQE.2003.819494
Michler, P. Quantum Dots in Quantum Photonics. (2017). https://doi.org/10.1007/978-3-319-56378-7.pdf.
Nenashev, A.V., Dvurechenskii, A.V.: Variational method of energy level calculation in pyramidal quantum dots. J. Appl. Phys. **10**(1063/1), 5143822 (2020)
Omran, H., Khalil, D.: Accessing rapidly scanning swept laser source instantaneous spectral width using a multimode rate equation model. IEEE J. Sel. Top. Quantum Electron. **21**(6), 714–721 (2015). https://doi.org/10.1109/JSTQE.2015.2443074

Petermann, K.: Calculated spontaneous emission factor for double-heterostructure injection lasers with gain-induced waveguiding. IEEE J. Quantum Electron. **15**(7), 566–570 (1979). https://doi.org/10.1109/JQE.1979.1070064

Petroff, P.M., DenBaars, S.P.: MBE and MOCVD growth and properties of self-assembling quantum dot arrays in III-V semiconductor structures. Superlatt. Microstruct. (1994). https://doi.org/10.1006/spmi.1994.1004

Pistol, M.E.: InP quantum dots in GaInP. J. Phys. Condens. Matter (2004). https://doi.org/10.1088/0953-8984/16/35/015

Porsche, J., Ruf, A., Geiger, M., Scholz, F.: Size control of self-assembled InP/GaInP quantum islands. J. Cryst. Growth **195**(1–4), 591–595 (1998). https://doi.org/10.1016/S0022-0248(98)00570-3

Porsche, J., Ost, M., Scholz, F., Fantini, A., Phillipp, F., Riedl, T., Hangleiter, A.: Growth of self-assembled InP quantum islands for red-light-emitting injection lasers. IEEE J. Select. Topics Quantum Electron. **6**(3), 482–490 (2000). https://doi.org/10.1109/2944.865103

Quirce, A., Virte, M.: nonlinear dynamics of semiconductor lasers and their applications. Nonlinear Dyn. Semicond. Lasers Appl. (2022). https://doi.org/10.3390/books978-3-0365-3509-8

Roßbach, R., Schulz, W.M., Eichfelder, M., Reischle, M., Beirne, G.J., Jetter, M., Michler, P.: Red to orange electroluminescence from InP/AlGaInP quantum dots at room temperature. J. Cryst. Growth **310**(23), 5098–5101 (2008). https://doi.org/10.1016/j.jcrysgro.2008.07.036

Schulz, W.M., Roßbach, R., Reischle, M., Beirne, G.J., Bommer, M., Jetter, M., Michler, P.: Optical and structural properties of InP quantum dots embedded in (Alx Ga1-x) 0.51 In0.49 P. Phys. Rev. B Condens. Matter Mater. Phys. **79**(3), 1–8 (2009). https://doi.org/10.1103/PhysRevB.79.035329

Schmidt, O. G., N. Kirstaedter, M-H. Mao, N. N. Ledentsov, D. Bimberg, V. M. Ustinov, A. Yu Egorov et al.: Overcoming gain saturation in InAs/GaAs quantum dot lasers. Conference Proceedings LEOS'96 9th Annual Meeting IEEE Lasers and Electro-Optics Society, Boston, MA, USA, 1996, pp. 324–325 vol. 1. https://doi.org/10.1109/LEOS.1996.565264.

Search, H., Journals, C., Contact, A., Iopscience, M., & Address, I.P. Self-organized growth of quantum-dot structures. 1365. (n.d.).

Sugawara, M., Mukai, K., Nakata, Y., Ishikawa, H., Sakamoto, A.: Effect of homogeneous broadening of optical gain on lasing spectra in self-assembled quantum dot lasers. Phys. Rev. B Condens. Matter Mater. Phys. **61**(11), 7595–7603 (2000). https://doi.org/10.1103/PhysRevB.61.7595

Wang, J., Sciarrino, F., Laing, A., Thompson, M.G.: Integrated photonic quantum technologies. Nat. Photon. **14**(5), 273–284 (2020). https://doi.org/10.1038/s41566-019-0532-1

Xiong, Y., Zhang, X.: InAs/InP quantum dots stacking: impact of spacer layer on optical properties. J. Appl. Phys. (2019). https://doi.org/10.1063/1.5082722

Zhang, Y., Wang, L., Wang, K., Wong, K.S., Wu, K.: Recent advances in the hardware of visible light communication. IEEE Access **7**(1), 91093–91104 (2019). https://doi.org/10.1109/ACCESS.2019.2927054

Zhou, Y., Duan, J., Grillot, F., Wang, C.: Optical noise of dual-state lasing quantum dot lasers. IEEE J. Quant. Electron. (2020). https://doi.org/10.1109/JQE.2020.3026090

Authors and Affiliations

Radwa A. Abbas[1,2] · Yasser M. Sabry[1] · Haitham Omran[2] · Zhihua Huang[3] · Michael Zimmer[3] · Michael Jetter[3] · Peter Michler[3] · Diaa Khalil[1]

✉ Radwa A. Abbas
radwa.khairy@guc.edu.eg

Yasser M. Sabry
yasser.sabry@eng.asu.edu.eg

Haitham Omran
haitham.omran@guc.edu.eg

Michael Zimmer
m.zimmer@ihfg.uni-stuttgart.de

Michael Jetter
m.jetter@ihfg.uni-stuttgart.de

Peter Michler
p.michler@ihfg.uni-stuttgart.de

Diaa Khalil
diaa_khalil@eng.asu.edu.eg

[1] Faculty of Engineering, Ain Shams University, 1 El-sarayat street, Abbassia, Cairo 11517, Egypt

[2] Laboratory of Micro-Optics, Faculty of Information Engineering and Technology (IET), German University in Cairo, Al Shabab Road, Cairo 11835, Egypt

[3] Institut für Halbleiteroptik und Funktionelle Grenzflächen (IHFG), Center for Integrated Quantum Science and Technology (IQST) and SCoPE, University of Stuttgart, 70569 Stuttgart, Germany